Settling the Magnetic Field Strength Debate in OMC-1

Arianna Imperiali

November 18, 2021

ABSTRACT

Studying magnetic fields across the Galaxy has become an essential part of understanding star formation and the role that magnetic support plays in gravitational cloud collapse. Recently, two distinguished groups, Guerra et al. (2021) and Hwang et al. (2021), have published separate works calculating the magnetic field strength for a region in our Galaxy, the Orion Molecular Cloud 1 (OMC-1). In each of these works, the Davis-Chandrasekhar-Fermi (DCF) method was employed to create maps of volume density, velocity dispersion, and angular polarization dispersion to ultimately calculate the magnetic field strength of the region. Guerra et al. (2021) found magnetic field strengths ranging from a few hundred μG to up to 2 mG. Hwang et al. (2021) found magnetic field strengths that vary from 0.8 to 24.6 mG. This paper analyzes the methods used by each group in calculating the angular polarization dispersion component of the DCF method to gauge whether or not it made a contribution to the large variation in magnetic field strength calculations. It was found that the angular polarization dispersion within OMC-1 calculated by Guerra et al. (2021) and Hwang et al. (2021) was quite different; therefore, we can conclude that the different methods used to calculate this component did have a significant effect on the resulting magnetic field strength calculations. This analysis provides invaluable input into gauging the reasons for the differences in results and will entice discussions about the accuracy of methods in calculating angular polarization dispersions.

1 Introduction

Far-Infrared (FIR) dust polarimetry has provided astronomers with new methods to study and map the distribution of magnetic fields in the diffuse Interstellar Medium (ISM) and molecular clouds throughout the Galaxy. Through a method known as radiative alignment torque, starlight can transfer angular momentum to dust grains, causing them to align their longest axes perpendicular to magnetic fields. This results in an observed polarization direction perpendicular to the magnetic field direction projected onto the plane of the sky (Lazarian & Hoang, 2007).

To determine large-scale magnetic field strength distributions in molecular clouds, Chandrasekhar & Fermi (1953) created the Davis-Chandrasekhar-Fermi (DCF) method. Hildebrand et al. (2009) and Houde et al. (2009) developed upon the DCF method to determine the dispersion of magnetic field vectors in turbulent molecular clouds The distortion of magnetic field lines by turbulence is reflected into the dispersion of the polarization angles (Hildebrand et al., 2009). Maps of magnetic field strength distributions can be produced through means of the DCF method by utilizing Eq. 1, which relates the magnetic field strength, B, to the volume density of the cloud, ρ, velocity dispersion of the gas coupled to the magnetic field, σ_v, and angular polarization dispersion of magnetic field vectors, σ_ϕ (Chandrasekhar & Fermi, 1953):

$$B^2 = 4\pi\rho\frac{\sigma_v^2}{\sigma_\phi^2}. \tag{1}$$

The Orion Molecular Cloud (OMC) is the closest sight of massive star formation, ∼ 390 pc away (Kounkel et al., 2017). Recently, two different authors, Guerra et al. (2021) and Hwang et al. (2021), obtained observations of a region in this cloud complex, OMC-1, which contains molecular gas and dust in the form of a ridge oriented roughly North-South (Guerra et al., 2021). On the West side of OMC-1, there is the BN object (a massive young stellar object) surrounded by the KL nebula (molecular gas and dust surrounding massive stars) (Becklin & Neugebauer, 1967; Kleinmann & Low, 1967) (to be referred to as the BNKL object throughout the rest of this paper). Southeast in the region is the Orion Bar, which bounds the HII region created by stars in the Trapezium Cluster and contains a photon-dominated region at the boundary between the HII region and molecular material (Chuss et al., 2019). The radiation emitted from these objects in OMC-1 affects dust grain alignment throughout the region (Lazarian & Hoang, 2007). Figure 1 depicts these three regions in OMC-1.

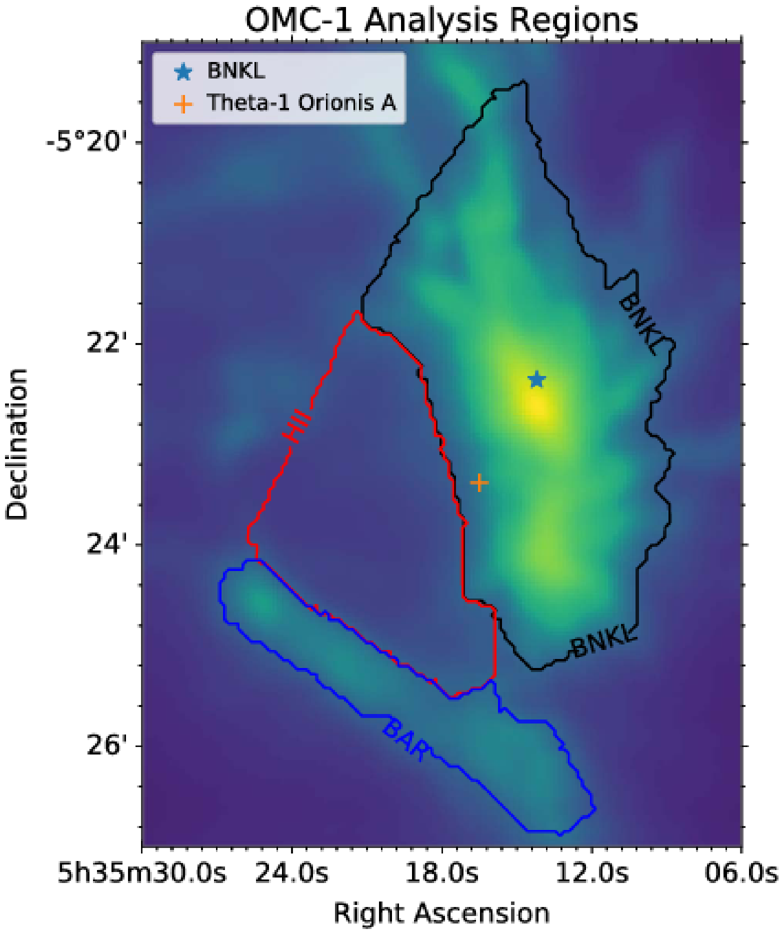

Figure 1: Three regions of OMC-1 are indicated by a black outline (BNKL), a red outline (HII region), and a blue outline (Orion Bar).

The objective of using dust polarimetry to map magnetic fields in OMC-1 is to better understand the relationship between the star formation process and gravitational collapse. Magnetic turbulence in molecular clouds regulates star forming activity in the ISM (Guerra et al., 2021). Astronomers who have previously mapped OMC-1 (e.g. Schleuning, 1998; Vallee & Bastien, 1999; Houde et al., 2004; Ward-Thompson et al., 2017) have found that the magnetic field in OMC-1 exhibits a pinch in the orthogonal direction to make an hourglass shape, which has been interpreted to indicate that the star formation in the OMC-1 region is magnetically regulated. Across magnetic field lines, gravitational collapse compresses the field lines to create regions of enhanced field strength; however, gravitational collapse can also be slowed by magnetic pressure (Guerra et al., 2021). Therefore, gauging whether a cloud will collapse depends on the relationship between mass and magnetic flux in the region.

Chuss et al. (2019) obtained photometry and polarimetry for the OMC-1 region using the High-resolution Airborne Wideband Camera (HAWC+) on board the Stratospheric Observatory for Infrared Astronomy (SOFIA). Measurements were taken at four different wavelengths in the FIR of 53, 89, 154, and 214 μm. Chuss et al. (2019) combined these observations with photometry within millimeter regimes to produce Spectral Energy Distributions (SEDs). Guerra et al. (2021) utilized these data to develop distribution maps corresponding to each of the components in Eq. 1. They first obtained a volume density map of molecular hydrogen by fitting the SEDs of infrared emission from OMC-1 in the range of 53 μm to 35 mm. They created a velocity dispersion map through the emission line spectra of the molecular tracer NH_3. NH_3 has been used as a probe of dense clouds, and the particular emission line transition (1,1), as described in Friesen et al. (2017), is highly correlated with dust column density. In order to produce the map of σ_ϕ^2, they applied a two-point structure function to the polarimetry data at each wavelength measurement within a small circular sub-region at each pixel. The maps of each component of Eq. 1 were then combined to produce maps of the magnetic field distribution along the plane-of-sky B_{POS} at each wavelength. B_{POS} values range from $\sim$100 μG to $\sim$ 2000 μG. The largest field strengths are consistently observed around and South of the BN/KL object while weaker field strengths are observed in the Bar region.

Hwang et al. (2021) obtained polarimetry and total intensity observations of OMC-1 with the POL-2 polarimeter on the Submillimetre Common-User Bolometer Array 2 (SCUBA-2) camera at 450 and 850 μm. This observation was a part of the James Clerk Maxwell Telescope (JCMT) program, B-fields in STar-forming Region Observations (BISTRO). They also used the Heterodyne Array Receiver Program (HARP) spectrometer to obtain the profiles of the $C^{18}O$ spectral lines. Hwang et al. (2021) estimated the volume density of molecular hydrogen from the continuum observations at 450 and 850 μm. They used the $C^{18}O$ spectral line profiles from HARP to measure the velocity dispersion. To find the polarization angle dispersion, they utilized the "unsharp masking" method similar to that used by Pattle et al. (2017). As described in Hwang et al. (2021), the team estimated a mean field orientation in a small 5" × 5" box in the region to trace its morphology. They moved the box over the entire region to obtain the distribution of mean field orientations. The collection of mean field directions traces large-scale variation of field lines, allowing for estimations of an angle dispersion between the original angle and estimated mean angles in a box. The angular dispersion is then a root-mean-square of the angle differences in the box. Similar to the process of Guerra et al. (2021), the three components of the DCF method were used to compose a map the magnetic field strength distribution in the region. They estimated a range of B_{POS} values from 0.8 to 26.4 mG at both 450 and 850 μm. The strongest field strength is observed to be in the region between the BN/KL object and the Southern part of OMC-1.

This paper will analyze the investigations completed by Guerra et al. (2021) and Hwang et al. (2021) to establish the reason for the order-of-magnitude difference in results. It is important to understand why there is such a large discrepancy so that the study of the magnetic fields in OMC-1 can be utilized for further projects regarding molecular cloud collapse and star formation. Section 2 reviews the HAWC+/SOFIA observations used in this work. Section 3 describes the implementation of the "unsharp masking" technique along with the calculation of the magnetic field strengths in each wavelength. Finally, a discussion of the results and implications are presented in Section 5.

2 Observations

2.1 HAWC+

Chuss et al. (2019) obtained photometry and polarimetry data of the OMC-1 region in December 2016 on Stratospheric Observatory for Infrared Astronomy (SOFIA) using the High-resolution Airborne Wideband Camera (HAWC+). With respect to the photometry data, raster scans of the region in all four bands observed, 53, 89, 154, and 214 μm, were done. The observing time per band ranged from 9 minutes for 53 μm to 2 minutes at 214 μm. Chuss et al. (2019) reduced the photometry data using CRUSH V2.4.2ALPHA1 with non-default reduction options. More specifically, they used the "bright" keyword to stop the possible clipping of data closer to the brighter regions, like the BN/KL object. Because of the relatively small fractional bandwidth of the filters, $\frac{\Delta\lambda}{\lambda} \approx .2$, they made no color corrections to the data. They adopted a 15% calibration uncertainty for the 53, 89, and 154 μm bands and 20% for the 214 μm band based on the variance of HAWC+ measurements.

Chuss et al. (2019) obtained additional polarimetry data in October-November 2017 and September 2018. Polarized light is represented by the Stokes parameters, I, Q and U. The data consist of maps of these Stokes parameters and their associated uncertainties for far-infrared (FIR) continuum emission at wavelengths of 53, 89, 154, and 214 μm. They were observed with nominal beam sizes of 4.9", 7.8", 13.6", and 18.2", respectively. These observations were done using the standard chop-nod-dither observing method (Harper et al., 2018). The chop throw ranged between 76 and 80, and the chop/nod angle was 125°, measured west of north. The observing times were approximately 3.5, 2.4, 0.5, and 0.5 hr at 53, 89, 154, and 214 μm, respectively. They reduced the data using the V1.3.0-BETA3 (April 2018) version of the HAWC+ data reduction pipeline. In order to merge the measurements into combined maps, they used relative background subtraction and smoothing with a Gaussian kernel having Full-Width Half-Max (FWHM) equal to half that of the diffraction-limited beam for each HAWC+ band (Harper et al., 2018); both of these are standard parts of the reduction pipeline.

3 Methodology

The methods used in calculating the angular polarization dispersion of the HAWC+ data sets were based on Pattle et al. (2017) and Hwang et al. (2021). Since in molecular clouds there are two main components to the measured magnetic field dispersion, turbulence and gravity, it is difficult to determine the local magnetic field dispersion directly from polarization observations (Hwang et al., 2021). Therefore, in order to measure the underlying field geometry, Pattle et al. (2017) estimated a mean field orientation in a small moving box throughout the OMC-1 region. By moving the box and estimating over the entire region, it was possible to trace the large-scale magnetic field over the entire region. Pattle et al. (2017) found good agreement between this moving box average and the true field direction using Monte Carlo simulations. They used a method analogous to the common image smoothing technique, 'unsharp masking.' We use 3x3, 5x5, and 7x7 pixel boxcar filters in the *convolve2d* function from Python's *SciPy* library to perform convolutions on the original Stokes U and Q maps to produce a smoothed map depicting the non-distorted magnetic field directions. We

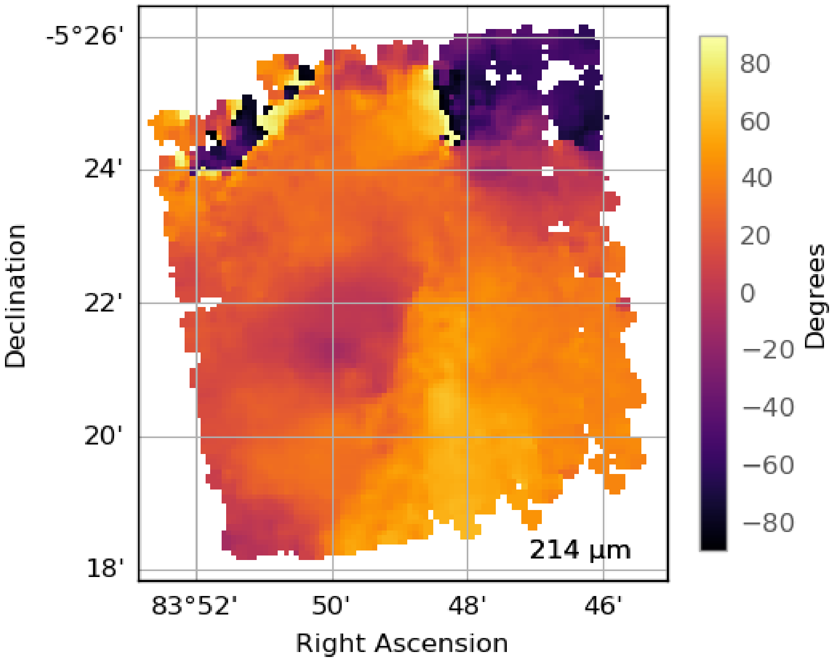

Figure 2: The observed angular differences map produced by using Eq. (2) on the Stokes U and Q maps.

measure the mean polarization angle θ of the original map before convolutions, as depicted in Eq. (2).

$$\theta = 0.5 * \arctan \frac{U}{Q}. \tag{2}$$

The obtained mean polarization angle is assigned to the central pixel of the box. This allows us to calculate the mean polarization angle of the smoothed map, as depicted in Eq. (3), where $\bar{U}$ and $\bar{Q}$ are the mean values averaged over the box.

$$\bar{\theta} = 0.5 * \arctan \frac{\bar{U}}{\bar{Q}} \tag{3}$$

Similar to Pattle et al. (2017), this calculation is repeated as the box moves over the entire image through convolutions, one pixel at a time. The smoothed map $\bar{\theta}$ is then subtracted from the observed map θ, resulting in a residual map $\delta\theta$ showing the deviation in angle of each pixel from the mean field direction, i.e. $\delta\theta_{i,j} = \theta_{i,j} - \bar{\theta}_{i,j}$ at pixel (i,j).

Figure 2 shows the observed angular position map, Figure 3 shows the smoothed angular position map, and Figure 4 shows the residual angular position map created with the 3x3 kernel for the 214 μm data set, as examples. From the residual map, we know an angular difference at each pixel, and we can calculate σ_ϕ as the standard deviation of the angular differences throughout the map for each kernel size for each of the four wavelengths Pattle et al. (2017) estimated the angular dispersion for the entirety of OMC-1. However, Hwang et al. (2021) suspected that each region would have a distinct B and that a single total estimate of B for the region as a whole would not be an accurate representation. Therefore, we incorporated object masks into this process to calculate the angular polarization value in the BN/KL region, the Trapezium Cluster, and the Orion Bar, as Hwang et al. (2021) did. When multiplied by the angular difference maps, these object masks

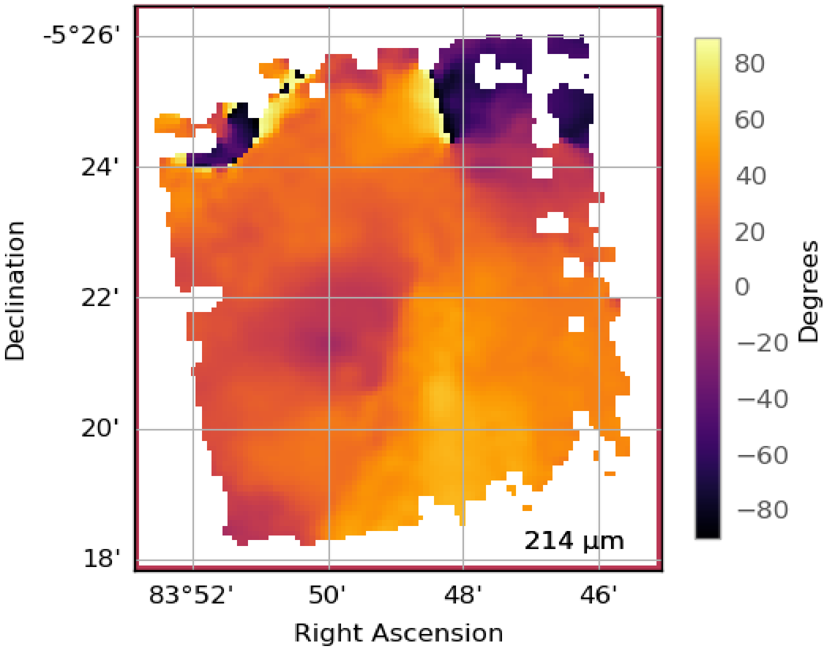

Figure 3: The smoothed angle differences map produced by Eq. (3) by applying convolutions with the 3x3 kernel size to the Stokes U and Q maps.

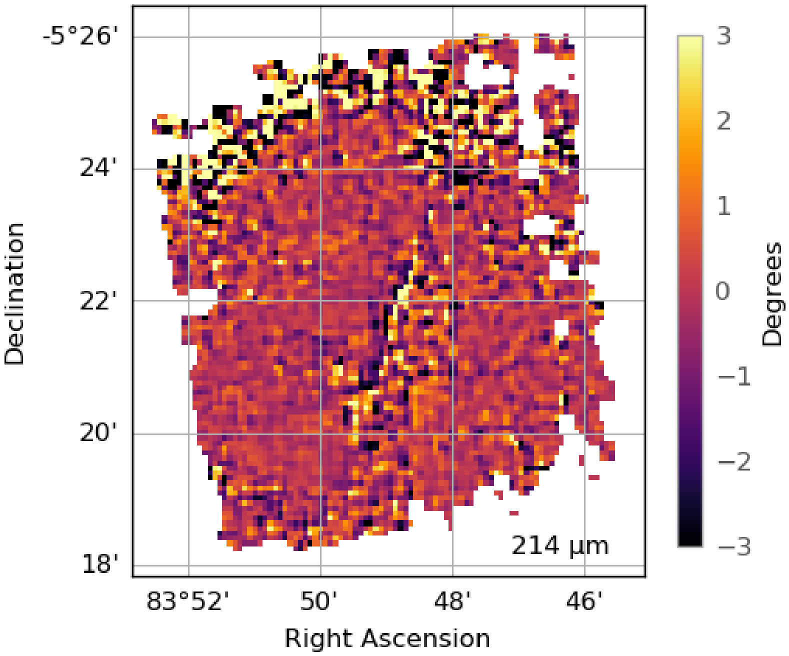

Figure 4: The resulting residual map by subtracting the smoothed map from the observed map.

Table 1: σ_ϕ (degrees)

Region	53 μm	89 μm	154 μm	214 μm
3x3 Kernel Size				
Bar	5.79	5.39	—	—
BNKL	2.34	1.90	2.80	2.72
HII	2.24	2.07	2.47	4.23
5x5 Kernel Size				
Bar	9.28	8.63	—	—
BNKL	3.63	2.96	4.82	3.75
HII	3.28	3.38	4.19	5.16
7x7 Kernel Size				
Bar	11.29	10.19	—	—
BNKL	4.41	4.04	5.94	4.79
HII	3.89	4.09	5.57	5.89

Table 2: N

	Bar	**BNKL**	**HII**
53 μm	8.50	6.67	24.59
89 μm	8.44	8.42	9.79
154 μm	—	5.02	19.32
214 μm	—	4.02	30.23

nullify all pixels not in the specified region, and we are able to calculate the standard deviation of each individual region. Table 1 lists σ_ϕ resulting from convolutions of each kernel size applied to each of the four wavelengths.

However, it is also important to consider the beam and line-of-sight integration that Chuss et al. (2019) incorporated into their analysis. To take this into account, we must utilize the number of turbulent cells in the gas column, N. N would therefore be accounted for by those cells that lie along the line-of-sight through the thickness of the cloud at any given point (Houde et al., 2009). Table 2 shows the N values for each region and wavelength and Table 3 shows the product of σ_ϕ and N, which are the values of σ_ϕ to be used for the rest of this analysis.

Once σ_ϕ was calculated for each wavelength for each kernel size, then we could insert those values into the DCF method in order to calculate the magnetic field strength. Chuss et al. (2019) calculated a uniform σ_v over the entire OMC-1 region as 1.85 km/s. To calculate ρ, they used the relationship in Eq. (4), where $N(H_2)$ is the average column density of molecular hydrogen (cm^{-2}), L is the uniform cloud depth (cm) over the entire OMC-1 region, μ is the mean molecular weight as determined by Sadavoy et al. (2013), and m_H is the atomic mass of hydrogen.

$$\rho = \frac{N(H_2)}{L}\mu m_H \tag{4}$$

Hwang et al. (2021) used the same L as calculated by Pattle et al. (2017), 4.34×10^{17} cm. The measured column density varied based on region. For the BN/KL object, the Trapezium Cluster, and the Orion Bar, the column densities are $(9.85 \pm 8.96) \times 10^{22}$ cm^{-2}, $(3.87 \pm 2.21) \times 10^{22}$ cm^{-2}, and $(5.90 \pm 3.24) \times 10^{21}$ cm^{-2}, respectively. Table 4 shows the final results of using Eq. (3) to compute the magnetic field strength values per region in each wavelength for each kernel size. It

Table 3: σ_ϕ ×N.

Region	53 μm	89 μm	154 μm	214 μm
3x3 Kernel Size				
Bar	.859	.793	—	—
BNKL	.272	.279	.245	.191
HII	.959	.352	.831	2.23
5x5 Kernel				
Bar	1.38	1.27	—	—
BNKL	.422	.435	.422	.263
HII	1.41	.575	1.41	2.72
7x7 Kernel				
Bar	1.67	1.50	—	—
BNKL	.513	.594	.520	.336
HII	1.67	.697	1.88	3.12

Table 4: B (μG)

Region	53 μm	89 μm	154 μm	214 μm
3x3 Kernel Size				
Bar	493	534	—	—
BNKL	2483	2425	2756	3544
HII	172	470	199	74
5x5 Kernel Size				
Bar	308	333	—	—
BNKL	1600	1554	1601	2570
HII	118	288	117	61
7x7 Kernel Size				
Bar	253	282	—	—
BNKL	1317	1137	1298	2009
HII	99	237	88	53

Table 5: B (μG) Results from Chuss et al. (2019)

	Bar	**BNKL**	**HII**
53 μm	303	1002	261
89 μm	289	931	316
154 μm	—	1013	305
214 μm	—	944	259

Table 6: $\frac{\langle B_t^2 \rangle}{\langle B_0^2 \rangle}$ and the Calculated σ_ϕ from Chuss et al. (2019)

Region	53 μm	89 μm	154 μm	214 μm
$\frac{\langle B_t^2 \rangle}{\langle B_0^2 \rangle}$				
Bar	1.61	1.77	—	—
BNKL	.370	.430	.370	.420
HII	.330	.230	.240	.340
σ_ϕ				
Bar	1.27	1.33	—	—
BNKL	.608	.656	.608	.648
HII	.574	.480	.490	.583

is important to note that the values for σ_ϕ and B of the Orion Bar for the 154 mm and 214 mm wavelength bands are not present in any table. This is because they were excluded from analysis as they were heavily influenced by systematic errors in the polarization vectors.

4 Discussion

The purpose of completing this analysis was to figure out if the means by which Hwang et al. (2021) and Guerra et al. (2021) calculated σ_ϕ was the primary reason for the large difference in B results for the OMC-1 region. Before we can complete analysis between the two different angular polarization dispersion methods, it was first necessary to convert the results from Chuss et al. (2019) into units which can be compared to the results obtained from this analysis. The dispersion function provided angular polarization in terms of a turbulent-to-ordered magnetic energy ratio. There is a relationship as given by Chuss et al. (2019) between the angular polarization σ_ϕ in degrees and the turbulent-to-ordered magnetic energy ratio $\frac{B_t^2}{B_0^2}$. The polarization angular dispersion results in units of degrees obtained for each HAWC+ data set were converted to this ratio, represented in Eq. (5):

$$\sigma_\phi^2 = \frac{\langle B_t^2 \rangle}{\langle B_0^2 \rangle} \tag{5}$$

Table 6 shows $\frac{\langle B_t^2 \rangle}{\langle B_0^2 \rangle}$ from Chuss et al. (2019) and its conversion to σ_ϕ so that it can be compared to the results from Table 3. Table 7 depicts the percent difference calculated for each angular polarization result, comparing those from Table 3 to those from Table 6. Additional analysis is needed to recognize which kernel size is most representative of the true results, so we applied the values from Chuss et al. (2019) to each of them for the purposes of this paper until we continue with this analysis. Upon looking at these results and their respective percent differences, it is apparent that the angular polarization values calculated using the 'unsharp masking' method and

Table 7: Percent Difference between σ_ϕ from Table 3 and Table 6.

Region	53 μm	89 μm	154 μm	214 μm
3x3 Kernel Size				
Bar	38.6	50.5	—	—
BNKL	76.3	80.8	85.1	109.1
HII	50.3	30.8	51.7	117.2
5x5 Kernel Size				
Bar	8.03	4.52	—	—
BNKL	36.1	40.5	36.1	84.6
HII	84.0	18.0	97.0	129.4
7x7 Kernel Size				
Bar	27.5	12.1	—	—
BNKL	17.0	9.93	15.5	63.3
HII	97.7	36.9	117.3	136.8

the dispersion function are not equal. This is indicative of the fact that there is indeed a significant difference in these analysis methods for the angular polarization component of the DCF method causing the large difference in B, as depicted in Table 4 and Table 5. However, in order to gauge whether or not there were contributions to this discrepancy from the data itself, the volume density component, or the velocity dispersion component, additional analysis is needed.

5 Acknowledgements

The author of this paper would like to acknowledge Jordan Guerra and David Chuss of the Villanova University Physics Department for acting as mentors throughout the duration of this research project. The author would also like to thank Joseph Michail and Catherine Petretti for help with the code. Finally, the author would like to acknowledge Michael Davis for the emotional torment that he has provided over the last three years.

References

Becklin, E. E., & Neugebauer, G. 1967, Apj, 147, 799

Chandrasekhar, S., & Fermi, E. 1953, apj, 118, 113. `https://ui.adsabs.harvard.edu/abs/1953ApJ...118..113C`

Chuss, D. T., Andersson, B. G., Bally, J., et al. 2019, Apj, 872, 187. https://arxiv.org/abs/1810.08233https://arxiv.org/abs/1810.08233

Friesen, R. K., Pineda, J. E., co-PIs, et al. 2017, Apj, 843, 63. https://arxiv.org/abs/1704.06318https://arxiv.org/abs/1704.06318

Guerra, J. A., Chuss, D. T., Dowell, C. D., et al. 2021, The Astrophysical Journal, 908, 98. `http://dx.doi.org/10.3847/1538-4357/abd6f0`

Harper, D. A., Runyan, M. C., Dowell, C. D., et al. 2018, Journal of Astronomical Instrumentation, 07, 1840008, doi: http://doi.org/10.1142/S225117171840008110.1142/S2251171718400081

Hildebrand, R. H., Kirby, L., Dotson, J. L., Houde, M., & Vaillancourt, J. E. 2009, The Astrophysical Journal, 696, 567–573. `http://dx.doi.org/10.1088/0004-637X/696/1/567`

Houde, M., Dowell, C. D., Hildebrand, R. H., et al. 2004, The Astrophysical Journal, 604, 717. `https://doi.org/10.1086/382067`

Houde, M., Vaillancourt, J. E., Hildebrand, R. H., Chitsazzadeh, S., & Kirby, L. 2009, Apj, 706, 1504. https://arxiv.org/abs/0909.5227https://arxiv.org/abs/0909.5227

Hwang, J., Kim, J., Pattle, K., et al. 2021, The Astrophysical Journal, 913, 85. `http://dx.doi.org/10.3847/1538-4357/abf3c4`

Kleinmann, D. E., & Low, F. J. 1967, Apj, 149, L1

Kounkel, M., Hartmann, L., Loinard, L., et al. 2017, The Astrophysical Journal, 834, 142. `https://doi.org/10.3847/1538-4357/834/2/142`

Lazarian, A., & Hoang, T. 2007, Monthly Notices of the Royal Astronomical Society, 378, 910

Pattle, K., Ward-Thompson, D., Berry, D., et al. 2017, The Astrophysical Journal, 846, 122. `http://dx.doi.org/10.3847/1538-4357/aa80e5`

Sadavoy, S. I., Francesco, J. D., Johnstone, D., et al. 2013, The Astrophysical Journal, 767, 126, doi: http://doi.org/10.1088/0004-637x/767/2/12610.1088/0004-637x/767/2/126

Schleuning, D. A. 1998, The Astrophysical Journal, 493, 811. `https://doi.org/10.1086/305139`

Vallee, J. P., & Bastien, P. 1999, The Astrophysical Journal, 526, 819. `https://doi.org/10.1086/308010`

Ward-Thompson, D., Pattle, K., Bastien, P., et al. 2017, The Astrophysical Journal, 842, 66. `https://doi.org/10.3847/1538-4357/aa70a0`